Assessing Passivity and Voltage-Stiffness of Grid-Forming Inverters via Black-Box Impedance

Sohail Ahmad Ali, *Student Member, IEEE*, Dang Duong Nguyen, *Student Member, IEEE*, Jingzhe Xu, *Student Member, IEEE*, Mohammad Hasan Ravanji, *Senior Member, IEEE*, Mehdi Ghazavi Dozein, *Senior Member, IEEE*, and Behrooz Bahrani, *Senior Member, IEEE*
Dept. of ECSE, Monash University, Melbourne, Australia
Corresponding author: Sohail A. Ali (sohail.ali@monash.edu)

***Abstract*—Most grid-code requirements defined by system operators require grid-forming (GFM) inverters to maintain a constant internal voltage phasor (IVP) behind an impedance; yet, the undefined location of the IVP introduces ambiguity across technologies. This paper develops analytical dq-frame models of three representative voltage-control strategies: proportional–integral (PI–VC), virtual-impedance (VI–VC), and virtual-admittance (VA–VC) control. It compares their performance in maintaining stability, voltage-source behavior (VSB), and passivity. Using analytical models and EMT-based impedance scans over the frequency range of 0.1–1000 Hz, the analysis reveals that enforcing passivity through higher virtual impedance inevitably weakens VSB. The results show that time-domain analysis alone cannot quantify GFM functionality, underscoring the need for impedance-based assessment. Finally, the study highlights that flexible control architectures with coordinated loop-shaping can simultaneously enhance closed-loop performance, VSB, and the passivity of the GFM inverter.**

***Index Terms*—Small-signal stability, voltage-source behavior, passivity, frequency-domain analysis, virtual impedance.**

I. Introduction

Grid-forming (GFM) inverter control has emerged as a cornerstone technology in the power system transition, owing to its ability to enhance withstand capabilities of inverter-based resources (IBRs) and to provide frequency and voltage support. Standards and guidelines issued by Transmission System Operators (TSOs) and international organizations, including those by UNIFI, AEMO, ENTSO-E, and NERC, define the required GFM capabilities [1]. Despite ongoing standardization efforts, ambiguity in defining GFM behavior continues to yield inconsistent interpretations among Original Equipment Manufacturers (OEMs). As discussed in [1], the term "near-constant internal voltage phasor (IVP)" remains ill-defined and may correspond to voltage regulation at the inverter terminal, the point of common coupling (PCC), or a virtual node. This lack of clarity has led to divergent voltage control philosophies across OEMs. Early implementations adopted proportional–integral vector voltage control (PI-VC) [2], whereas the WECC/UNIFI generic models—developed in collaboration with Tesla, SMA, and GE Vernova—standardized a virtual-impedance-based voltage control (VI-VC) approach [3], [4]. More recently, Siemens introduced a virtual-admittance-based voltage control (VA-VC) scheme for HVDC GFM inverters [5], and Hitachi applied a similar concept in GFM STATCOM design [6]. This difference in the interpretations of the GFM requirement may lead to unpredictable transient behavior.

Instabilities continue to arise from converter interactions [7]. With proprietary control implementations limiting model access, stability assessment must remain compatible with black-box systems. The Generalized Nyquist Criterion (GNC) has therefore become a widely used tool [8], but its conclusions depend on grid conditions that shift as the network evolves. Passivity-based design is increasingly viewed as a future-compatible approach since it guarantees stability when two passive, standalone-stable subsystems are interconnected [9]. As a result, emerging grid-code proposals are starting to mandate the passivity of GFM impedance over specified frequency ranges [10]. However, no existing study quantitatively compares stability, voltage-source behavior (VSB), and passivity across voltage controllers. Therefore, the contributions of this work are as follows:

1) Analytical dq-frame terminal-impedance models of three popular voltage-control schemes are derived and validated against EMT-based frequency scans,
2) Stability across varying short-circuit ratios (SCRs) is assessed using eigenvalue analysis and the GNC,
3) VSB is quantified based on the singular values of the terminal impedance [11], and passivity is evaluated by checking the positive definiteness of the impedance matrix [12].

As will be shown in this work, an inherent trade-off exists between increasing terminal impedance to achieve passivity and maintaining the low impedance required for strong VSB. While expanding the dissipative region of GFM inverters enhances system stability, it also diminishes voltage stiffness. This trade-off poses a critical challenge for TSOs and OEMs: how can both passivity and strong voltage-stiffness characteristics be realized concurrently?

The remainder of this paper is organized as follows. Section II introduces the three GFMI control schemes and their analytical small-signal model (SSM). Section III examines SCR-dependent stability using eigenvalue and GNC analysis. Section IV compares VSB and passivity, and Section V summarizes the findings and outlines coordinated loop-shaping strategies to reconcile both objectives.

979-8-3315-8138-1

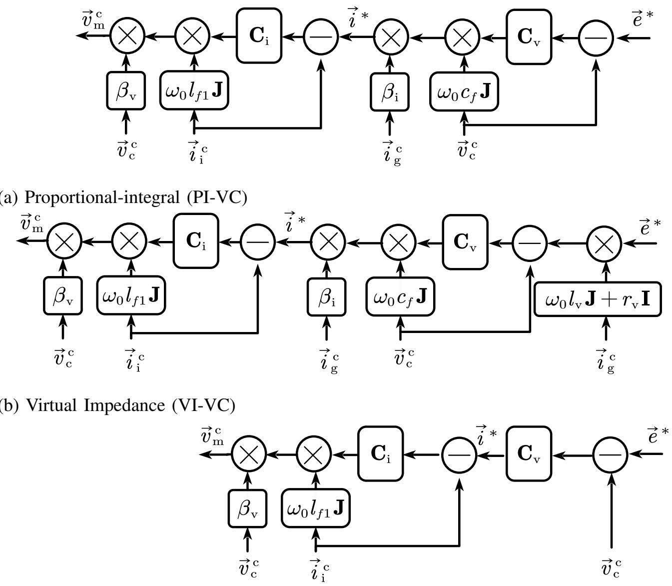

(a) Proportional-integral (PI-VC)

(b) Virtual Impedance (VI-VC)

(c) Virtual Admittance (VA-VC)

Fig. 1. Three grid-forming voltage control structures represented in the dq-frame (e.g., $\vec{v}_{\mathrm{m}}^{\mathrm{c}} = [v_{\mathrm{m,d}}^{\mathrm{c}},\ v_{\mathrm{m,q}}^{\mathrm{c}}]^{\top}$ indicates d- and q-axis components in converter frame). The operator "×" generalizes summation and subtraction operations in the decoupling terms.

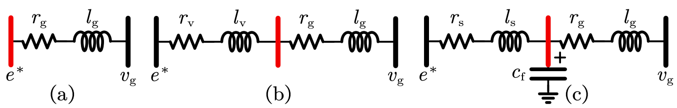

Fig. 2. Equivalent steady-state circuit model of (a) PI, (b) VI, and (c) VA-based GFM. The PCC (shown in red) is the point at which VSB and passivity are evaluated.

II. System Description and Small-Signal Modeling of GFM with Different Voltage Control Strategies

The voltage control with proportional-integral (PI-VC) shown in Fig. 1a is widely used for voltage regulation and disturbance rejection. However, increased grid strength can trigger sub-synchronous oscillations and tuning is complicated for devices with low switching frequency [13]. To overcome these issues, recent approaches introduce a fictitious impedance between IVP and PCC, forming the basis of virtual-impedance (VI-VC) [14] and virtual-admittance (VA-VC) [15] control schemes, illustrated in Figs. 1b and 1c, respectively. Their steady-state effect is shown in Fig. 2, where the added impedance clearly affects static power-transfer capability and reactive-power support for remote faults. However, comparing dynamic stability, VSB, and passivity in black-box systems requires a frequency domain model of the terminal impedance.

As shown in our earlier work, the Component Connection Method (CCM) provides a modular way to construct SSMs of GFM. Building on the framework proposed in [13], the analytical model of the terminal impedance is derived. Throughout this section, variables in the converter reference frame use the superscript $(\cdot)^c$, while variables in the system (grid) frame use $(\cdot)^s$. Bold symbols denote matrices (e.g., $\mathbf{W}$). The imaginary-unit matrix is $\mathbf{J} = [0, -1;\ 1, 0]$ and the identity matrix is $\mathbf{I} = [1, 0;\ 0, 1]$. Starting from the internal control, the inverter terminal voltage $\vec{v}_{\mathrm{i}}^{c}$ is a delayed version of the modulating voltage reference $\vec{v}_{\mathrm{m}}^{\mathrm{c}}$, represented using a third-order Padé approximation as $\vec{v}_{\mathrm{i}}^{c} = \mathbf{G}_{\mathrm{d}}(s)\vec{v}_{\mathrm{m}}^{\mathrm{c}}$. The current control law that generates $\vec{v}_{\mathrm{m}}^{\mathrm{c}}$ is

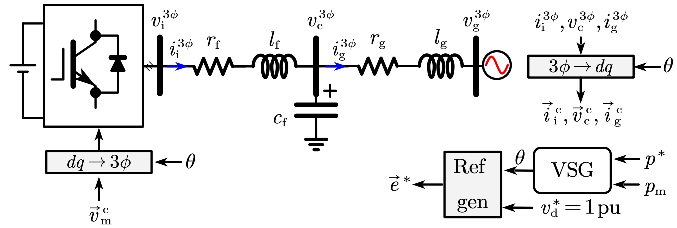

Fig. 3. GFM inverter controlled as a PV bus using a virtual synchronous generator-based active power loop. Signal measurement and outer-loop structures are consistent across all three voltage-control schemes.

TABLE I. Benchmark parameters.

Variable	Value	Description	Variable	Value	Description
Inverter & control parameters			**Grid parameters**		
s_{rated}	1 MVA	Inverter rated power	v_{g}	0.69kV	Grid voltage (L-L)
f_{sw}	20 kHz	Switching frequency	f_{g}	50 Hz	Nominal frequency
v_{dc}	1.3 kV	DC link voltage	**Proportional-Integral VC**		
l_{f}	0.1 pu	Inverter-side inductor	$k_{\mathrm{p}v}$	3.3 pu	Proportional gain
c_{f}	0.05 pu	Filter capacitor	$k_{\mathrm{i}v}$	176 pu/s	Integral gain
$k_{\mathrm{p}i}$	0.48 pu	CC proportional gain	**Virtual Impedance VC**		
$k_{\mathrm{i}i}$	1.5 pu/s	CC integral gain	l_{v}	0.1 pu	Virtual inductor
β_{v}	1	Voltage feedforward gain	r_{v}	0 pu/s	Virtual resistor
β_{i}	0.8	Current feedforward gain	**Virtual Admittance VC**		
m_{p}	0.017 pu	$P-\omega$ Droop gain	l_{s}	0.2 pu	Virtual inductor
h_{v}	5 s	Inertial time constant	r_{s}	0.07 pu/s	Virtual resistor

$$\vec{v}_{\mathrm{i}}^{\mathrm{c}} = \mathbf{G}_{\mathrm{d}}\left[\mathbf{C}_{\mathrm{i}}\left(\vec{i}^{*} - \vec{i}_{\mathrm{i}}^{\mathrm{c}}\right) + \omega_o l_{\mathrm{f}}\mathbf{J}\vec{i}_{\mathrm{i}}^{\mathrm{c}} + \beta_{\mathrm{v}}\vec{v}_{\mathrm{c}}^{\mathrm{c}}\right], \tag{1}$$

where $\mathbf{C}_i = [k_{\mathrm{p}i} + k_{\mathrm{i}i}/s]\mathbf{I}$. The three voltage controllers are developed based on the structures shown in Fig. 1, and parametrized according to the values presented in Table I. The PI-VC in Fig. 1a follows a form similar to the CC, with its dynamics expressed as:

$$\vec{i}^{*} = \mathbf{C}_{\mathrm{v}}\left(\vec{e}^{*} - \vec{v}_{\mathrm{c}}^{\mathrm{c}}\right) + \omega_{\mathrm{o}} c_{\mathrm{f}}\mathbf{J}\vec{v}_{\mathrm{c}}^{\mathrm{c}} + \beta_{\mathrm{i}}\vec{i}_{\mathrm{g}}^{\mathrm{c}}, \tag{2}$$

where $\mathbf{C}_v = [k_{\mathrm{p}v} + k_{\mathrm{i}v}/s]\mathbf{I}$.

The VI-VC in Fig. 1b uses the same inner-loop PI-based voltage control, but it regulates a fictitious voltage $\vec{v}_{\mathrm{f}}$ behind the virtual impedance: $\vec{v}_{\mathrm{f}} = \vec{v}_{\mathrm{c}}^{\mathrm{c}} + \mathbf{Z}_{\mathrm{VI}}\vec{i}_{\mathrm{g}}^{\mathrm{c}}$, where $\mathbf{Z}_{\mathrm{VI}} = [l_{\mathrm{v}}\omega_{\mathrm{o}}\mathbf{J} + r_{\mathrm{v}}\mathbf{I}]$. The VI-VC dynamics are expressed as:

$$\vec{i}^{*} = \mathbf{C}_{\mathrm{v}}\left(\vec{e}^{*} - \vec{v}_{\mathrm{f}}\right) + \omega_{\mathrm{o}} c_{\mathrm{f}}\mathbf{J}\vec{v}_{\mathrm{c}}^{\mathrm{c}} + \beta_{\mathrm{i}}\vec{i}_{\mathrm{g}}^{\mathrm{c}}. \tag{3}$$

The VA-VC method in Fig. 1c emulates a dynamic inductor without requiring derivatives. The VA-VC dynamics are given by:

$$\vec{i}^{*} = \mathbf{Y}_{\mathrm{VA}}\left(\vec{e}^{*} - \vec{v}_{c}^{\mathrm{c}}\right), \tag{4}$$

where, $\mathbf{Y}_{\mathrm{VA}} = \left[l_{\mathrm{s}}\left(s\mathbf{I} + \omega_{\mathrm{o}}\mathbf{J}\right) + r_{\mathrm{s}}\mathbf{I}\right]^{-1}$.

By substituting $\vec{i}^{*}$ from (2)–(4) into (1), the general relationship of inner control to $\vec{v}_i$ can be obtained. The explicit derivation is shown only for the VI-VC case, which contains the most interconnections. The PI-VC and VA-VC expressions

979-8-3315-8138-1

follow directly by considering the respective $\mathbf{C}_\mathrm{v}$. This yields the inner-control loop as a subsystem:

$$\vec{v}_\mathrm{i}^\mathrm{c} = \mathbf{G}_\mathrm{d}\mathbf{C}_\mathrm{i}\mathbf{C}_\mathrm{v}\vec{v}_\mathrm{err} + \omega_\mathrm{o}c_\mathrm{f}\mathbf{J}\mathbf{G}_\mathrm{d}\mathbf{C}_\mathrm{i}\vec{v}_\mathrm{c}^\mathrm{c} + \beta_\mathrm{i}\mathbf{G}_\mathrm{d}\mathbf{C}_\mathrm{i}\vec{i}_\mathrm{g}^\mathrm{c} - \mathbf{C}_\mathrm{i}\vec{i}_\mathrm{i}^\mathrm{c} + \omega_\mathrm{o}l_\mathrm{f}\mathbf{J}\vec{i}_\mathrm{i}^\mathrm{c} + \beta_v\vec{v}_\mathrm{c}^\mathrm{c}, \tag{5}$$

where, $\vec{v}_\mathrm{err} = \vec{e}^* - \vec{v}_\mathrm{f}$. To make the inner control–circuit relationship easier to interpret, the LC filter dynamic is expressed in the converter frame as:

$$\vec{v}_\mathrm{i}^\mathrm{c} = l_\mathrm{f}(s\mathbf{I} + \omega_\mathrm{o}\mathbf{J})\left[c_\mathrm{f}(s\mathbf{I} + \omega_\mathrm{o}\mathbf{J})\,\vec{v}_\mathrm{c}^\mathrm{c} + \vec{i}_\mathrm{g}^\mathrm{c}\right] + \vec{v}_\mathrm{c}^\mathrm{c}, \tag{6}$$

$$\vec{i}_\mathrm{i}^\mathrm{c} = c_\mathrm{f}(s\mathbf{I} + \omega_\mathrm{o}\mathbf{J})\,\vec{v}_\mathrm{c}^\mathrm{c} + \vec{i}_\mathrm{g}^\mathrm{c}. \tag{7}$$

Substituting for $\vec{v}_\mathrm{i}^\mathrm{c}$ and $\vec{i}_\mathrm{i}^\mathrm{c}$ from (6) and (7), respectively, into (5) yields the closed-loop dynamics of the cascaded controller. Since the system is linear-time invariant (LTI), its SSM is obtained by replacing all variables with their perturbations as:

$$\Delta\vec{v}_\mathrm{c}^\mathrm{c} = \boldsymbol{G}_{\mathrm{e}^*\to\mathrm{v_c}}(s)\Delta\vec{e}^* + \boldsymbol{Z}_\mathrm{o}^\mathrm{c}(s)\Delta\vec{i}_\mathrm{g}^\mathrm{c}. \tag{8}$$

In (8), $\mathbf{G}_{e^*\to v_c}(s)$ denotes the closed-loop VC response, while $\mathbf{Z}_\mathrm{o}^\mathrm{c}(s)$ captures the influence of current disturbances on $\vec{v}_\mathrm{c}^\mathrm{c}$. Clearly, the effect of current perturbation is minimized when $\mathbf{Z}_\mathrm{o}^\mathrm{c}$ is small. A simplified version of (8) is given in [16], but it neglects fast dynamics and excludes power-control effects, making it valid approximately in the range 10–100 Hz. The full matrix expressions are omitted here, as they serve only as internal subsystems within the CCM formulation. In (8), the input vector is $\vec{u_\mathrm{ctrl}} = [\Delta\vec{e}^*,\ \Delta\vec{i}_\mathrm{g}^\mathrm{c}]^\top$ and the output vector is $\vec{y_\mathrm{ctrl}} = \Delta\vec{v}_\mathrm{c}^\mathrm{c}$.

To capture the effect of angle perturbations, the active-power control (APC) loop is modeled using the governor equation of a Virtual Synchronous Generator (VSG). The linearized APC dynamics are

$$\Delta\theta = \frac{\omega_\mathrm{o}}{s}C_\mathrm{APC}\left(\Delta p^* - \Delta p_\mathrm{m}\right), \tag{9}$$

where $C_\mathrm{APC} = \left[2h_\mathrm{v}s + \frac{1}{m_\mathrm{p}}\right]^{-1}$, input vector $\vec{u}_\mathrm{APC} = [\Delta p^*,\ \Delta p_\mathrm{m}]^\top$, and output vector $\vec{y}_\mathrm{APC} = \Delta\theta$. The converter and system reference frames are related through the linearized transformation

$$\begin{aligned}\Delta v_\mathrm{c,d}^\mathrm{s} &= \Delta v_\mathrm{c,d}^\mathrm{c} - v_\mathrm{c,q0}\Delta\theta, & \Delta v_\mathrm{c,q}^\mathrm{s} &= \Delta v_\mathrm{c,q}^\mathrm{c} + v_\mathrm{c,d0}\Delta\theta,\\ \Delta i_\mathrm{g,d}^\mathrm{c} &= \Delta i_\mathrm{g,d}^\mathrm{s} + i_\mathrm{g,q0}\Delta\theta, & \Delta i_\mathrm{g,q}^\mathrm{c} &= \Delta i_\mathrm{g,q}^\mathrm{s} - i_\mathrm{g,d0}\Delta\theta.\end{aligned} \tag{10}$$

The active-power perturbation is obtained from the linearized active power expression

$$\Delta p_\mathrm{m} = \left\langle \vec{i}_\mathrm{g0}^\mathrm{s}, \Delta\vec{v}_\mathrm{c}^\mathrm{s}\right\rangle + \left\langle \vec{v}_\mathrm{c0}^\mathrm{s}, \Delta\vec{i}_\mathrm{g}^\mathrm{s}\right\rangle, \tag{11}$$

where $<,>$ is the vector inner product operator. Based on this, the non-unified model of the GFM is shown in Fig. 4a. To obtain the GFM impedance, including APC dynamics, the relational matrices $\mathbf{R}_{uy}$, $\mathbf{R}_{uu}$, $\mathbf{R}_{yy}$, and $\mathbf{R}_{yu}$ for CCM are defined as [13]

$$\begin{aligned}\Delta\vec{u}_\mathrm{s,ol} &= \mathbf{R}_{uy}\Delta\vec{y}_\mathrm{s,ol} + \mathbf{R}_{uu}\Delta\vec{u}_\mathrm{ol},\\ \Delta\vec{y}_\mathrm{ol} &= \mathbf{R}_{yy}\Delta\vec{y}_\mathrm{s,ol} + \mathbf{R}_{yu}\Delta\vec{u}_\mathrm{ol},\end{aligned} \tag{12}$$

where the stacked subsystem input and output vectors are $\vec{u}_\mathrm{s,ol} = [\vec{u}_\mathrm{ctrl}^\top,\ \vec{u}_\mathrm{APC}^\top]^\top$ and $\vec{y}_\mathrm{s,ol} = [\vec{y}_\mathrm{ctrl}^\top,\ \vec{y}_\mathrm{APC}^\top]^\top$. The

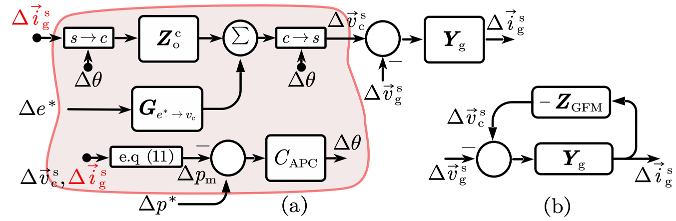

Fig. 4. SSM as (a) non-unified model of GFM and (b) interconnected impedance forming closed-loop feedback. Red denotes exogenous input.

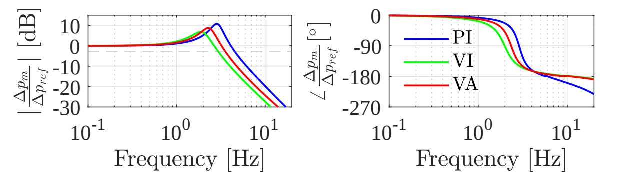

Fig. 5. Comparing the closed-loop response of power control for different VCs at SCR=10.

unified system input and output are selected as $\vec{u}_\mathrm{ol} = \Delta\vec{i}_\mathrm{g}^\mathrm{s}$ and $\vec{y}_\mathrm{ol} = \Delta\vec{v}_\mathrm{c}^\mathrm{s}$, while the active-power and voltage references are treated as constants (i.e., $\Delta p^* = \Delta e^* = 0$). The open-loop SSM of the GFM is expressed as

$$\Delta\dot{\vec{x}}_\mathrm{ol} = \mathbf{A}_\mathrm{ol}\,\Delta\vec{x}_\mathrm{ol} + \mathbf{B}_\mathrm{ol}\,\Delta\vec{u}_\mathrm{ol}, \tag{13}$$

$$\Delta\vec{y}_\mathrm{ol} = \mathbf{C}_\mathrm{ol}\,\Delta\vec{x}_\mathrm{ol}, \tag{14}$$

where $\mathbf{A}_\mathrm{ol}$, $\mathbf{B}_\mathrm{ol}$, and $\mathbf{C}_\mathrm{ol}$ are block-diagonal matrices containing the dynamics of the inner-control subsystem and the APC. Finally, the impedance of the GFM is obtained from (14) as

$$-\mathbf{Z}_\mathrm{GFM}(s) = \mathbf{C}_\mathrm{ol}\,(s\mathbf{I} - \mathbf{A}_\mathrm{ol})^{-1}\mathbf{B}_\mathrm{ol}. \tag{15}$$

The grid dynamics are defined in the system frame as

$$\frac{\Delta\vec{i}_\mathrm{g}^\mathrm{s}}{\Delta\vec{v}_\mathrm{c}^\mathrm{s} - \Delta\vec{v}_\mathrm{g}^\mathrm{s}} = Y_g = \frac{1}{l_\mathrm{g}\,(s\mathbf{I} + \omega_\mathrm{o}\mathbf{J}) + r_\mathrm{g}\mathbf{I}}. \tag{16}$$

Finally, based on (15) and grid model in (16), the closed-loop SSM can be established as a feedback loop shown in Fig. 4.

III. Stability Assessment via Eigenvalue and Generalized Nyquist Criterion

The $\mathbf{C}_\mathrm{v}$ in PI-VC and VI-VC is tuned to about 150 rad/s (one-tenth of the CC bandwidth), to meet sub-transient VC requirements. In contrast, VA–VC is expected to regulate the PCC voltage through slower outer loop, analogous to an automatic voltage control (AVR) in synchronous generators (SGs). For a fair comparison, all controllers employ the same outer power loop, as shown in Fig. 3, and are tuned to achieve consistent closed-loop power-control dynamics [16], as illustrated in Fig. 5. The PI–VC and VI–VC designs follow [13], while the VA–VC follows [16]. To ensure compatibility with black-box systems, the analytically derived impedance in (15) is validated against the EMT model impedance obtained through a multi-sine frequency sweep. As shown in Fig. 6, all three GFM inverter models closely match in the frequency range of 0.1–1000 Hz, confirming their adequacy for subsequent stability, VSB, and passivity assessments. Fig. 7 illustrates the evolution of the closed-loop poles with increasing SCR for the

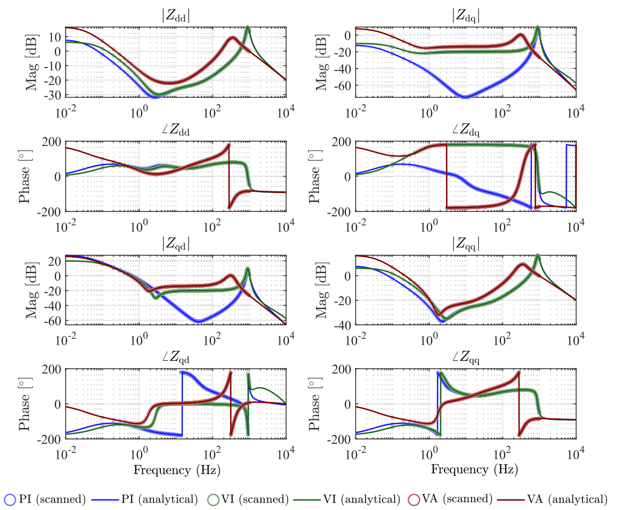

Fig. 6. Comparison between analytical and measured $\mathbf{Z}_{\mathrm{GFM}}(j\omega)$ for different VC-based GFM inverters. The impedances are measured while connected to the grid of SCR=10 and operating at $p^* = 1$ p.u and $E^* = 1$ p.u.

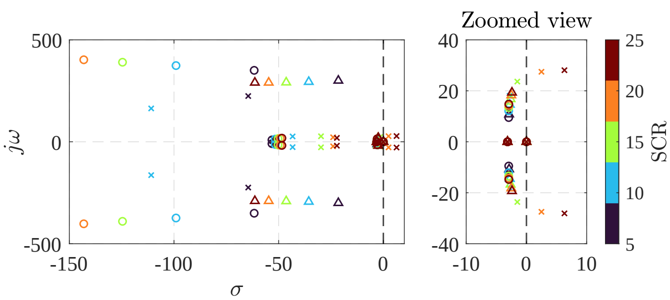

Fig. 7. Eigenvalue trajectories of different VC-based GFM inverters as grid strength varies (SCR=[5,25]). Markers: ×-PI, ○-VI, △-VA.

three voltage controllers. These results are consistent with the GNC validation in Fig. 8. The PI-VC exhibits a loss of stability beyond SCR $= 20$, indicated by eigenvalue migration into the right-half plane. On the other hand, each Nyquist plot displays the collection of two eigenvalue trajectories of the minor-loop gain $-\mathbf{Y}_g\mathbf{Z}_{\mathrm{GFM}}$ on the complex plane. An encirclement of the critical point $(-1, j0)$ appears for the PI-VC in Fig. 8a, which indicates that the feedback loop is unstable. VI-VC and VA-VC are stable since no encirclement is observed. The time-domain responses in Fig. 9 corroborate the frequency-domain analysis: the PI-VC becomes unstable for SCR > 20, producing a 4 Hz oscillation.

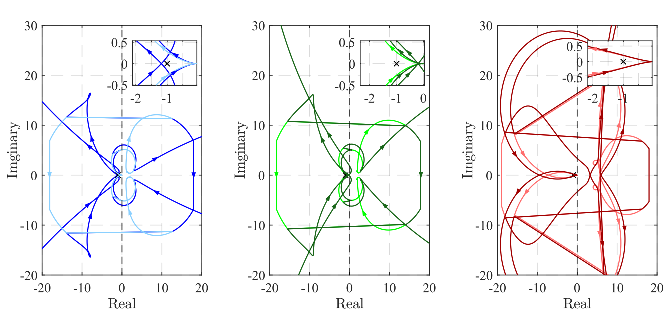

(a) PI (b) VI (c) VA

Fig. 8. Stability assessment using GNC for different VCs at SCR=20.

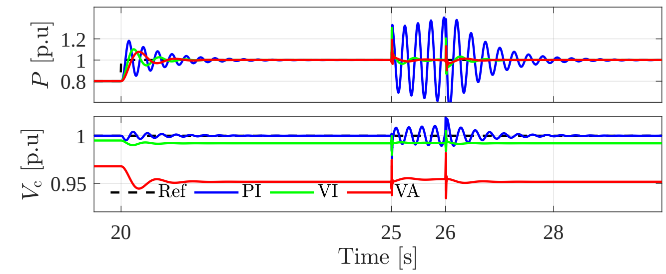

Fig. 9. Time-domain comparison of active power and PCC voltage magnitude for the three VC strategies under a 0.2 pu active power reference perturbation at $t = 20$ s. The SCR is increased from 15 to 20 at $t = 25$ s and reduced back to 15 at $t = 26$ s.

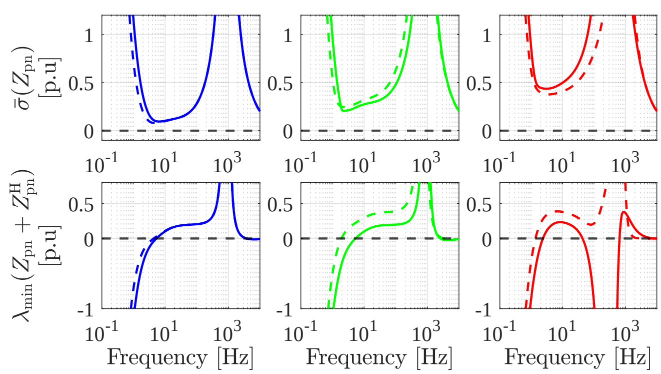

(a) PI (b) VI (c) VA

Fig. 10. Effect of loop shaping to simultaneously achieve passivity and VSB. Solid lines denote the benchmark cases and dashed lines denote the passivified versions. (a) PI: $h_{\mathrm{v}}(5s \rightarrow 10s)$, (b) VI: $r_{\mathrm{v}}(0 \rightarrow 0.05$ p.u.), and (c) VA: $\beta_{\mathrm{v}}(1 \rightarrow 0)$.

IV. Voltage Source Behavior and Passivity Assessment

A GFM inverter is regarded as an effective voltage source behind an impedance, where a lower series impedance corresponds to stiffer voltage regulation, particularly around 5∼150 Hz. The dq-frame impedance cross-coupling is reduced by converting into the modified positive–negative sequence impedance representation [17]. Following the approach in [11], the VSB is evaluated using the singular value of the impedance matrix, i.e., $\bar{\sigma}(\mathbf{Z}_{\mathrm{pn}}(j\omega))$. A large singular value indicates deviation from an ideal VSB.

In parallel, passivity is assessed following the method [12], where the instantaneous power dissipation of the inverter, defined with the current flowing from the inverter to the grid, is expressed as $-(v^H i + i^H v) = i^H[\mathbf{Z}_{\mathrm{pn}}(j\omega) + \mathbf{Z}_{\mathrm{pn}}^H(j\omega)]i$ where v and i are complex phasors of voltage and current, and $(.)^H$ denotes the Hermitian transpose. The inverter is dissipative and, therefore, passive if the matrix $[\mathbf{Z}(j\omega)+\mathbf{Z}^H(j\omega)]$ is positive definite for all frequencies, which holds when $\lambda_{\min}[\mathbf{Z}_{\mathrm{pn}}(j\omega) + \mathbf{Z}_{\mathrm{pn}}^H(j\omega)] > 0, \forall\omega \in [0, \infty]$.

Fig. 10 shows the influence of parameters on VSB and passivity. The objective is to maintain a strong VSB within the frequency range of 5–150 Hz to increase the generalized-SCR [11] and to extend the dissipative region up to the Nyquist

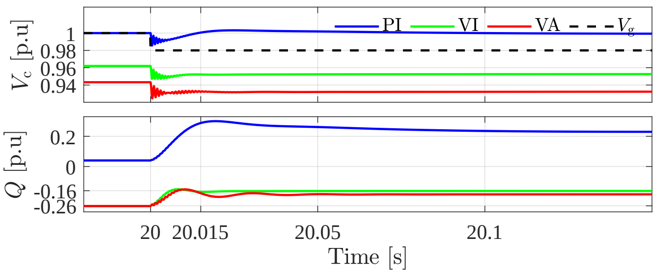

Fig. 11. Time-domain comparison of PCC voltage and reactive power response to a 2 % grid-voltage sag at $t = 20$ s.

limit ($0 - f_{\mathrm{sw}}/2$). All structures remain non-passive at low frequencies, similar to SGs. Increasing h_{v} enhances voltage stiffness by resisting rapid angle deviations, strengthening VSB at low frequencies. Raising r_{v} broadens the positive-dissipation region and improves stability margins but weakens VSB. The VA-VC achieves the widest dissipative bandwidth but the narrowest VSB range, as $\bar{\sigma}(\mathbf{Z}(j\omega))$ exhibits the smallest flat region compared to the PI- and VI-VCs, owing to its larger inherent impedance. A narrow non-passive pocket appears near the filter resonance, which can be suppressed by disabling β_{v}; however, as noted in [13], this diminishes closed-loop CC performance and limits current protection capability. These results emphasize the fundamental trade-off where straightforwardly increasing passivity may compromise VSB. Nevertheless, the differing sensitivities of h_{v}, r_{v}, and β_{v} indicate that coordinated loop-shaping can balance both objectives, i.e., achieving wide-band passivity while retaining strong voltage-source characteristics. The time-domain comparison in Fig. 11 supports this interpretation, showing the system response to a voltage disturbance after applying the passivating loop-shaping described in Fig. 10.

Under a 2% voltage sag, all three GFM inverters inject reactive power within 15 ms, satisfying dynamic grid-support requirements. However, the magnitude differs markedly: the VA–VC, owing to its higher output impedance and lower VSB, provides substantially less reactive support than the PI–VC in the first cycle. Only the PI–VC restores the PCC voltage to 1 p.u., underscoring that increasing virtual impedance to improve stability in strong grids can undermine voltage recovery during faults and in weak grids.

V. Conclusion

This paper presents a unified framework for evaluating the VSB–passivity trade-off in GFM inverters based on black-box impedance. It shows that while stiff VSB improves voltage regulation, it can introduce low-frequency oscillations under strong-grid conditions. Conversely, enforcing passivity through higher virtual impedance enhances stability but weakens VSB.

The following key points can be concluded from this study: First, improved stability may come at the expense of closed-loop performance, VSB, or passivity. Moreover, time-domain analysis provides little quantitative insight into how closely different structures operate to their stability margins. Consequently, TSOs should adopt impedance-based characterization as the primary method for assessing GFM functionality. Second, although the compared controllers cannot simultaneously satisfy multiobjective requirements on performance, VSB, and passivity, OEMs may employ flexible higher-order control architectures that enable coordinated loop-shaping to balance these objectives.

Finally, while this study established a basis for comparing the trade-off between VSB–passivity using black-box impedance, it does not yet define a quantitative threshold for what constitutes a "good" GFM. Developing such technology-agnostic criteria remains an important direction for future work.

References

[1] A. Gupta, B. Chaudhuri, and M. O'Mally, "Revisiting the Definition of Grid-Forming Inverter-Based Resources," *TechRxiv*, pp. 1–180, 2025.

[2] A. Yazdani and R. Iravani, *Voltage-Sourced Converters in Power Systems*. John Wiley & Sons, Ltd, 2010.

[3] W. Du, S. G. Vennelaganti, and D. Ramasubramanian, "Model Specifications of Grid-Forming Hybrid Control and Plant Control—REGFM_C1 and REPCGFM_C1," UNIFI, Tech. Rep., 2025.

[4] M. Ali and W. Sarah, "Megapack Grid-Forming Enabling Simplicity and Flexibility in BESS Projects," Tesla, Tech. Rep., 2025. [Online]. Available: https://www.esig.energy/wp-content/uploads/2024/01/ESIG_GFM_Tesla_Rev0.pdf

[5] S. Karrari *et al.*, "White paper: Grid-forming converters – advantages of grid-forming control in hvdc and facts applications," Siemens Energy, Tech. Rep., 2024, online; accessed 2024. [Online]. Available: https://www.siemens-energy.com/global/en/home/publications/white-paper/download-grid-forming-converters.html

[6] J.-P. Hasler, C. Danielsson, T. Soong, L. Bessegato, and L. Harnefors, "Grid-forming control for power electronic converter devices," Patent Application WO2 022 262 952A1, December, 2022, international Publication Number WO 2022/262952 A1. [Online]. Available: https://patentscope.wipo.int/search/en/detail.jsf?docId=WO2022262952

[7] X. Xiaorong, "Analysis and control of oscillatory stability in renewable power systems: China's experience," IEEE-PELS-Technical Committee Webinar Programme, April 2024.

[8] N. Mohammed, H. Udawatte, W. Zhou, D. J. Hill, and B. Bahrani, "Grid-forming inverters: A comparative study of different control strategies in frequency and time domains," *IEEE Open Journal of the Industrial Electronics Society*, vol. 5, pp. 185–214, 2024.

[9] J. C. Willems, "Dissipative dynamical systems part i: General theory," *Archive for Rational Mechanics and Analysis*, vol. 45, no. 5, pp. 321–351, 1972. [Online]. Available: https://doi.org/10.1007/BF00276493

[10] 50 Hertz and Amprion and Tennet and TransnetBW, "4-TSO Paper onRequirements for Grid-Forming Converters," Tech. Rep., 2025.

[11] H. Xin, C. Liu, X. Chen, Y. Wang, E. Prieto-Araujo, and L. Huang, "How many grid-forming converters do we need? a perspective from small signal stability and power grid strength," *IEEE Transactions on Power Systems*, vol. 40, no. 1, pp. 623–635, 2025.

[12] F. Chen, X. Wang, L. Harnefors, S. Z. Khong, D. Wang, L. Zhao, K. C. Sou, M. Routimo, J. Kukkola, H. Sandberg, and K. H. Johansson, "Limitations of using passivity index to analyze grid–inverter interactions," *IEEE Transactions on Power Electronics*, vol. 39, no. 11, pp. 14 465–14 477, 2024.

[13] S. A. Ali, P. Serna-Torre, P. Hidalgo-Gonzalez, M. G. Dozein, and B. Bahrani, "Modularized small-signal modeling of grid-forming inverters," *IEEE Access*, vol. 13, pp. 97 011–97 037, 2025.

[14] X. Wang, Y. W. Li, F. Blaabjerg, and P. C. Loh, "Virtual-impedance-based control for voltage-source and current-source converters," *IEEE Transactions on Power Electronics*, vol. 30, no. 12, pp. 7019–7037, 2015.

[15] P. Rodriguez, I. Candela, and A. Luna, "Control of pv generation systems using the synchronous power controller," in *2013 IEEE Energy Conversion Congress and Exposition*, 2013, pp. 993–998.

[16] Y. Xiao, H. Luo, Y. Yang, H. Ruan, M. Molinas, F. Blaabjerg, and K.-H. Loo, "Low-frequency oscillation mechanism and mitigation in grid-forming inverters with voltage controller effects," *IEEE Transactions on Industry Applications*, pp. 1–15, 2025.

[17] A. Rygg, M. Molinas, E. Unamuno, C. Zhang, and X. Cai, "A simple method for shifting local dq impedance models to a global reference frame for stability analysis," *arXiv preprint arXiv:1706.08313*, 2017. [Online]. Available: https://arxiv.org/abs/1706.08313

979-8-3315-8138-1